Materials Today Communications 52 (2026) 115211

Contents lists available at ScienceDirect

Materials Today Communications

journal homepage: www.elsevier.com/locate/mtcomm

Fabrication of Ni-SiC composite coating with coral-like hierarchical structure via magnetic field-assisted jet electrodeposition for efficient oil/water separation

Ya Chen [a,b], Haozhe Pang [a], Shimao Shangguan [a], Wuxin Yang [b,*], Jianfeng Zhao [a], Sarat Singamneni [c], Zongjun Tian [a,*]

[a] College of Mechanical and Electrical Engineering, Nanjing University of Aeronautics and Astronautics, Nanjing 210016, China
[b] Department of Chemical and Materials Engineering, The University of Auckland, Auckland 1010, New Zealand
[c] Department of Mechanical Engineering, AUT University, Auckland 1010, New Zealand

ARTICLE INFO

Keywords:
Underwater superoleophobic
Ni-SiC
Jet electrodeposition
Magnetic-field
Oil/water separation

ABSTRACT

A Ni-SiC composite coating was effectively synthesized on a stainless-steel substrate through a jet electrodeposition technique integrated with a magnetic field, and then utilized for oil/water separation. Guided by an external magnetic field, the magnetically responsive nickel components loaded with hydrophilic SiC were incorporated into the coating, creating a coral-like micro-nano hierarchical rough structure. The functionalized mesh demonstrated remarkable superhydrophilic properties and submerged low-adhesion superoleophobicity. Appropriate processing parameters were identified by analyzing how electrodeposition duration and voltage influence the surface topography as well as the wettability associated with the Ni-SiC-coated mesh. The results indicated that the Ni-SiC-coated mesh prepared at 30 V for 10 min exhibited a WCA of 0° and a UOCA of 152.2°. Ni-SiC-coated meshes fabricated at a lower voltage required a deposition time of 30 min to achieve superhydrophilicity and underwater superoleophobicity. The mesh achieved high efficiency along with superior purification levels for various oil/water emulsions and sustained a stable separation performance (exceeding 95%) after 50 cycles. The treated substrate maintained its functionality in aggressive media. In natural conditions, the Ni-SiC-coated mesh still retained its outstanding superhydrophilicity and underwater superoleophobicity after three months of storage. In addition, the Ni-SiC-coated mesh maintained a UOCA of more than 150° after water erosion for 10 h.

1. Introduction

Industrial and domestically generated oily wastewater severely affects ecosystems and human health [1–3]. It is widely recognized that these complications can be effectively resolved through the oil/water separation process. However, traditional oil/water separation methods are limited because of unfavorable characteristics, including suboptimal separation performance, exorbitant running expenses, susceptibility to incidental contamination, and intricate execution procedures [4]. Thus, exploiting an efficient and economical method to treat oily wastewater is necessary and urgent.

Materials endowed with unique wetting behaviors show contrasting affinities for oils and water, paving the way for novel separation methodologies [5]. Over the past few years, "oil-selective" substances characterized by superhydrophobic/superoleophilic properties have gained significant attention [6,7]. Nevertheless, these interfaces often suffer from clogging or degradation when exposed to viscous crude oils [8,9]. Mimicking the underwater oleophobicity observed in fish scales, researchers have pioneered "water-selective" surfaces that merge superhydrophilicity with underwater superoleophobicity [10,11]. Such systems facilitate the creation of a robust hydration shield, which precludes the attachment of oily residues. To date, these functional interfaces have been synthesized via diverse protocols, including chemical etching [12], hydrothermal [13], electrospinning [14], chemical vapor deposition [15], and layer-by-layer assembly [16]. Furthermore, electrodeposition has become a prevalent method because of its cost-effectiveness, procedural simplicity, and excellent batch-to-batch reliability [17,18]. Compared with conventional methods, jet

* Corresponding authors.
E-mail addresses: wuxin.yang@auckland.ac.nz (W. Yang), tianzj@nuaa.edu.cn (Z. Tian).

https://doi.org/10.1016/j.mtcomm.2026.115211
Received 7 March 2026; Received in revised form 12 April 2026; Accepted 17 April 2026
Available online 17 April 2026

electrodeposition technology offers enhanced liquid-phase mass transport. This advancement substantially suppresses concentration polarization while promoting higher limiting current densities, which collectively bolsters the efficiency of the coating process [19,20]. Nevertheless, few research has been conducted on using jet electrodeposition for the synthesis of superhydrophilic/underwater superoleophobic mesh substrates.

Studies have shown that the combination of surface chemistry with high surface energy and micro/nano hierarchical structures contributes to the superhydrophilicity of a material [21]. Thus, the synthesis of superhydrophilic coatings uses nanoparticles characterized by high surface energy. For example, Gondal et al. [22] constructed surfaces with superhydrophilic and underwater superoleophobic properties by atomizing nanostructured TiO_2 onto stainless steel mesh frameworks. Gunatilake et al. [23] demonstrated the fabrication of high-performance coatings by applying natural and hydrothermally processed mica onto stainless steel mesh, achieving simultaneous superhydrophilicity and underwater superoleophobicity. Nickel coatings are widely used in industrial products and protective coatings because of their corrosion resistance and chemical stability [24,25]. Recent studies reported the synthesis of nickel-coated meshes possessing superhydrophilic properties for use in oil/water separation processes [17,26]. However, previous studies [27] showed that the nickel-coated meshes spontaneously adsorb low-surface-energy organics in the air, thereby losing superhydrophilicity. As a type of hydrophilic ceramic filler, nano-sized SiC particles show outstanding oxidation resistance, robust mechanical performance, and superior chemical stability [28]. It is expected to prepare stable superhydrophilic/underwater superoleophobic meshes by incorporating nano-SiC particles into nickel coatings.

In this work, jet electrodeposition with a magnetic field was applied to fabricate Ni-SiC composite coating meshes. Under the influence of an external magnetic field, the Ni-SiC composite particles were deposited in the coating and formed a coral-like micro-nano hierarchical structure on the mesh. The forming process of the micro-nano structure was analyzed. Further investigation revealed that the surface morphology and wettability of the Ni-SiC-coated mesh were significantly affected by the electrodeposition time and voltage. The functionalized mesh demonstrated exceptional wettability, featuring simultaneous underwater superoleophobicity and superhydrophilicity. This enabled the gravity-driven purification of various oil/water mixtures with high efficiency. The prepared superhydrophilic mesh can be used repeatedly at least 50 times and exhibits stability in acidic, alkaline, brine, and natural environments.

2. Experimental setup

2.1. Materials

Stainless steel meshes were applied as cathode substrates in the electrodeposition. The composite particles were mixed with Nickel nanoparticles (500 nm) and SiC nanoparticles (150 nm) using a planetary ball mill with a 5:1 mass ratio. The morphology and XRD pattern of Ni-SiC composite particles are demonstrated in Fig. 1. SiC particles were mixed with Ni particles by stirring in a planetary ball mill. Hexane, silicone oil, kerosene, liquid paraffin, and dichloromethane (DCE) were obtained from Shanghai Aladdin Biochemical Technology Co., Ltd as oil resources in the oil/water separation test. The composition of the electrolyte used in the experiments of magnetic field-assisted jet electrodeposition is listed in Table 1. All reagents in this study are analytical-grade.

2.2. Experimental device

Fig. 2 illustrates the magnetic field-assisted jet electrodeposition, where an adjustable pump delivers the electrolyte into the anode cavity to be ejected through a 2 mm × 30 mm rectangular nozzle. A nickel rod serves as a soluble anode within the cavity to replenish consumed nickel ions, while the conductive electrolyte jet completes the electrical circuit between the anode and cathode. During the process, the nozzle executes a cyclic reciprocating motion across the cathode mesh, facilitating uniform coating deposition under DC power excitation. A water bath maintains the electrolyte at a constant temperature, and a magnet block positioned beneath the cathode fixture provides a uniform magnetic field perpendicular to the cathode surface.

2.3. Processing of Ni-SiC composite coating

Before electrodeposition, the stainless-steel mesh (35 mm × 35 mm) was ultrasonically cleaned with ethanol for 10 min, and then washed with deionized water. A constant magnetic field of 50 mT was

Table 1
Composition of electrolyte.

Chemicals	Content
$NiSO_4{\cdot}6\ H_2O$	260 g/L
$NiCl_2{\cdot}6\ H_2O$	40 g/L
H_3BO_3	40 g/L
$C_7H_5O_3NS$	5 g/L
Ni-SiC	1 g/L

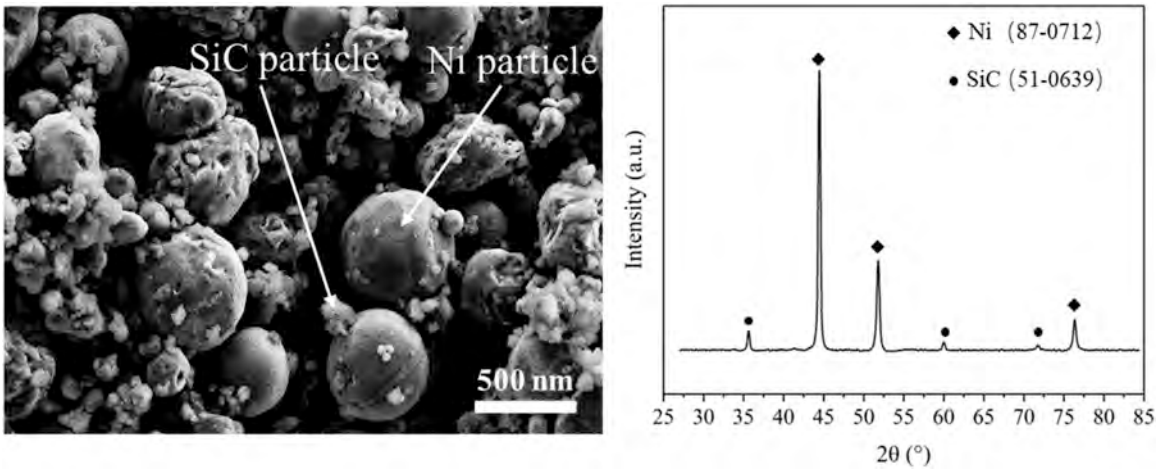

Fig. 1. Morphology and XRD pattern of Ni-SiC particles.

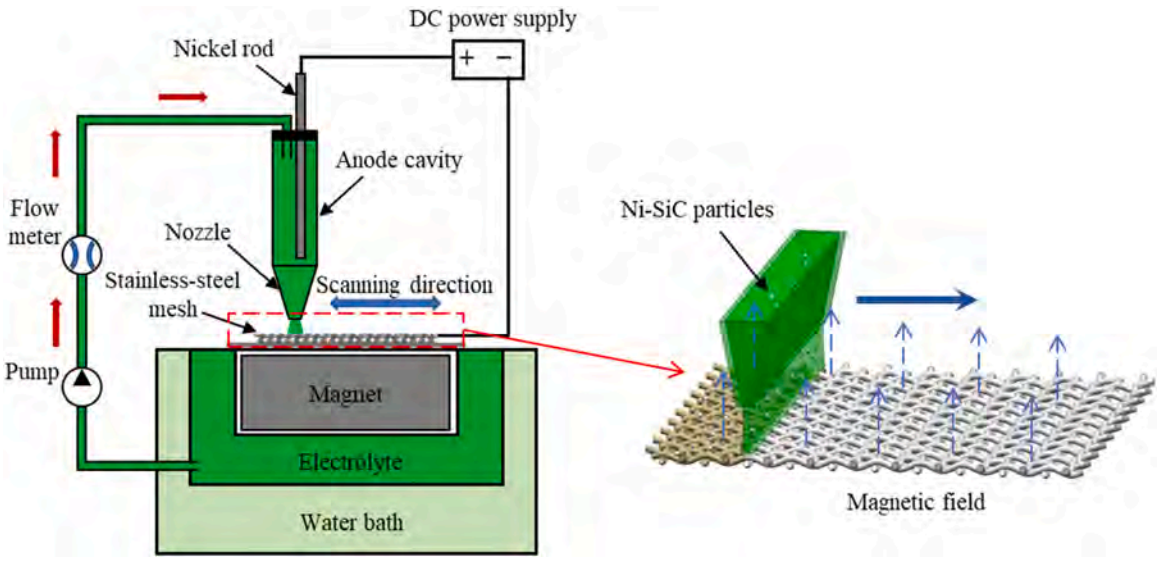

Fig. 2. Experimental setup illustration and processing detail of magnetic field-assisted jet electrodeposition.

maintained by aligning the magnet so that the flux lines were perpendicular to the cathode surface. The scanning range of the nozzle was 30 mm, and a Ni-SiC composite coating with a dimension of 30×30 mm^2 was formed. Specific settings for the magnetic field-assisted jet electrodeposition were listed in Table 2.

2.4. Samples characterization

The surface and cross-section morphologies of stainless-steel mesh and coatings were captured by the scanning electron microscope (SEM, JSM-6360LV, Japan). The chemical composition of the electrodeposited coatings was detected with the energy dispersive spectroscopy (EDS, X-MAX, Oxford Instruments, UK). The phase distribution and grain orientation of Ni-SiC composite particles were characterized by an X-ray diffraction (XRD, Ultima IV, Japan). The scanning rate of XRD was 10°/min. Water contact angle (WCA) and underwater oil contact angle (UOCA) were tested with the sessile drop method through the contact angle goniometer (OCA50AF, Dataphysics, Germany) at ambient temperature. Underwater adhesion testing was conducted using a polytetrafluoroethylene (PTFE) tube to manipulate the oil droplet (DCE, 5 μL). The organic content of the collected filtrate was measured using a total organic carbon (TOC) analyzer (Multi N/C 3100, Analytik Jena, Germany).

2.5. Experiments of oil/water separation

In the experiment of oil/water separation, hexane, kerosene, silicone oil, liquid paraffin, and DCE were used to verify the separation behavior of different oils. Before the experiment, the materials were wetted in the deionized water. The oil/water separation equipment was assembled by clamping the prepared mesh between two quartz glass tubes with an inner diameter of 16 mm. For easier observation, Sudan I was added to the oil, and methylene blue was added to the water. An oil/water emulsion (1:1 ratio) was supplied from the inlet of the device, where the permeated water phase was subsequently recovered and measured after passing through the Ni-SiC-coated mesh. The oil/water separation efficiency is calculated by Eq. (1) [29]:

$$\eta = (m_1/m_0) \times 100\% \quad (1)$$

where m_1 and m_0 are the weights of oil before and after separation, respectively.

The oil/water separation ability of the superhydrophilic mesh was measured by the oil intrusion pressure and water permeation flux. [30]. The oil intrusion pressure is determined by the maximum oil layer height that the Ni-SiC-coated mesh can accommodate. When the oil pressure is less than the intrusion pressure, the oil cannot permeate the Ni-SiC-coated mesh. The oil intrusion pressure is calculated by Eq. (2):

$$P = \rho g h_{max} \quad (2)$$

where ρ denotes the density of the oil, g represents the acceleration of gravity, and h_{max} is the maximum height in the tube of the oil that the mesh can support.

The water permeation flux is determined according to Eq. (3):

$$F = V/St \quad (3)$$

where V is the volume of permeating water, S denotes the effective separation area, and t is the time required for water to completely permeate the mesh.

Table 2
Key parameters for magnetic field-assisted jet electrodeposition.

Experimental parameters	Content
Applied voltage	10, 20, 30 V
Deposition time	10, 20, 30 min
Gap between electrodes	2 mm
Scanning speed	4 mm/s
Magnetic flux density	50mT
Flow rate	150 L/h
Temperature	40 ± 5 °C
pH	4.0 ± 0.5

3. Results and discussion

3.1. Surface morphology and chemical composition

The SEM morphologies of the blank mesh and the coatings are shown in Fig. 3. The pore size of the blank mesh was approximately 50 μm with a smooth and delicate texture (Fig. 3a-c). After electrodeposition, the wire surface was densely decorated, and the roughness was enhanced. Magnetic field-assisted electrodeposition facilitated the formation of hierarchical coral-like clusters through nanoparticle accumulation. The average pore size of the mesh decreased to 40 μm (Fig. 3d and e). In addition, the cross-sectional morphology of the mesh revealed that a nickel film with a nominal thickness of 2.2 μm was deposited onto the mesh surface, as shown in Fig. 3f. However, Fig. 3g-i presented that the

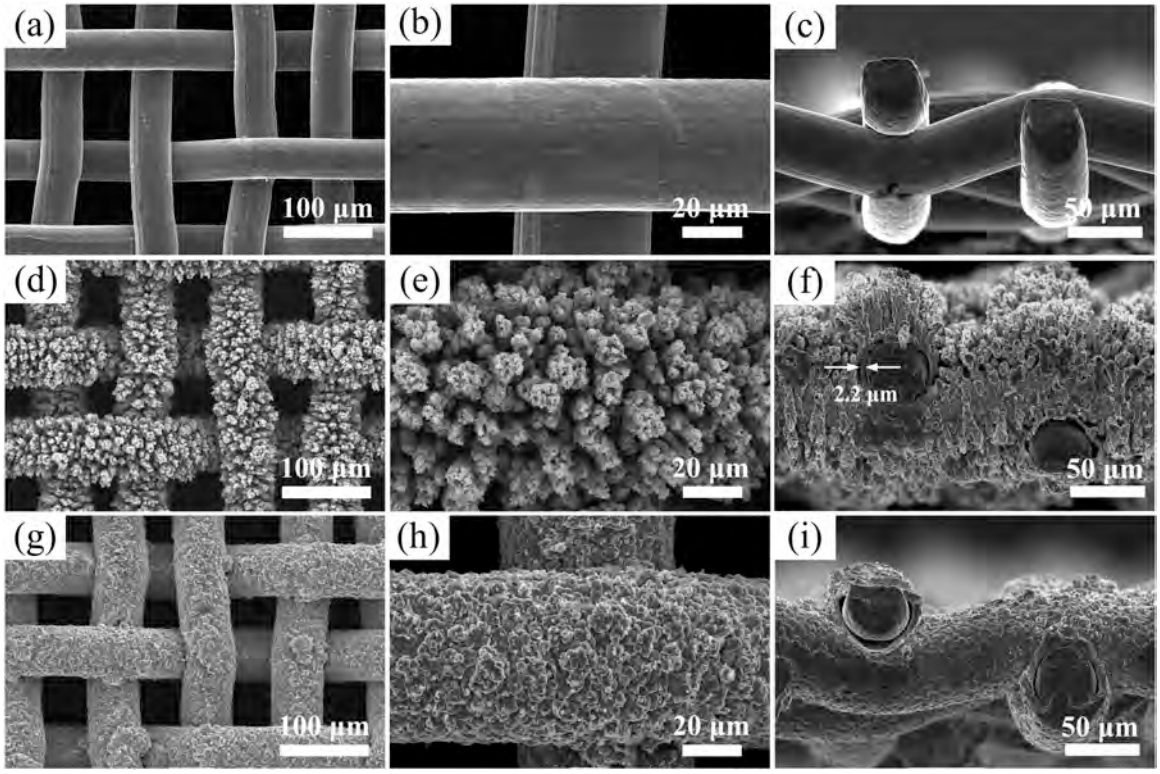

Fig. 3. Surface and cross-sectional morphology of (a-c) blank mesh; (d-f) Ni-SiC composite coating mesh prepared with a magnetic field; (h-i) Ni-SiC composite coating mesh prepared without a magnetic field.

mesh surface was relatively flat and only a few nanoparticles were adsorbed without applying a magnetic field, suggesting that the coral-like micro-nano multiscale morphology was primarily governed by the introduction of an external magnetic field during the coating process.

The EDS spectrum of the Ni-SiC composite coating mesh is presented in Fig. 4a. Elemental analysis revealed the existence of C and Si on the mesh interface, evidencing the successful integration of the SiC phase. Elevated carbon concentrations compared to silicon were observed, resulting from the spontaneous sequestering of atmospheric hydrocarbons by the active coating [31]. Element mappings of Ni, C, and Si are shown in Fig. 4b. The uniform distribution of these elements across the images confirmed that the Ni-SiC composite particles were evenly deposited on the mesh surface.

3.2. Analysis of forming process

Fig. 5 illustrates the deposition mechanism of the Ni-SiC composite coating. During the initial stage of jet electrodeposition, the high current density promotes the rapid formation of a primary nickel film on the mesh substrate. Under a steady external magnetic field, both the pre-deposited Ni film and the suspended Ni-SiC particles become magnetized, developing opposing magnetic poles (Fig. 5a). The resulting magnetic attraction pulls the Ni-SiC particles toward the mesh surface. Guided by the principle of energy minimization, these particles align and distribute themselves along the magnetic flux lines (Fig. 5b). Simultaneously, Ni ions in the electrolyte are reduced at the interface, creating a continuous nickel matrix that embeds and secures the particles within the growing composite layer (Fig. 5c).

The transition from simple deposition to a complex coral-like hierarchical structure is driven by the synergy of magnetic attraction and repulsion. As deposition progresses, the Ni-SiC components preferentially stack parallel to the magnetic field. This coalescence leads to the development of prominent peak-like formations, mirroring the spiked topographical "Rosensweig instability" characteristic of ferrofluids

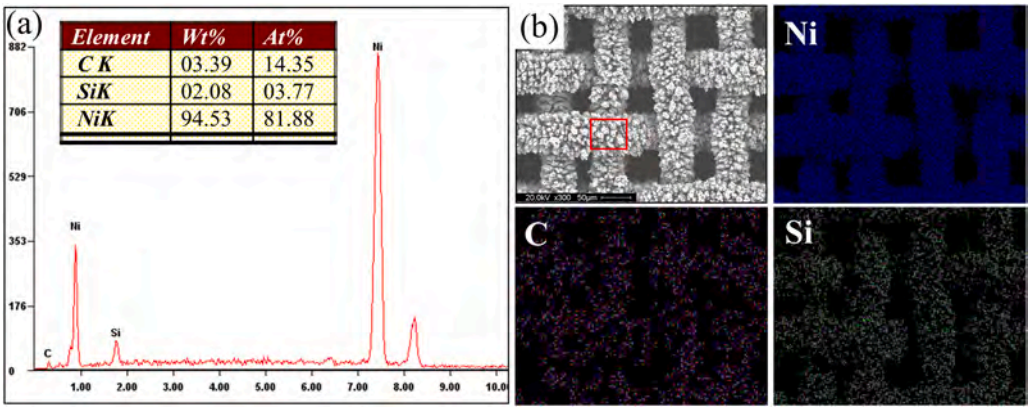

Fig. 4. (a) EDS spectrum and (b) elemental mapping of the Ni-SiC composite coating mesh.

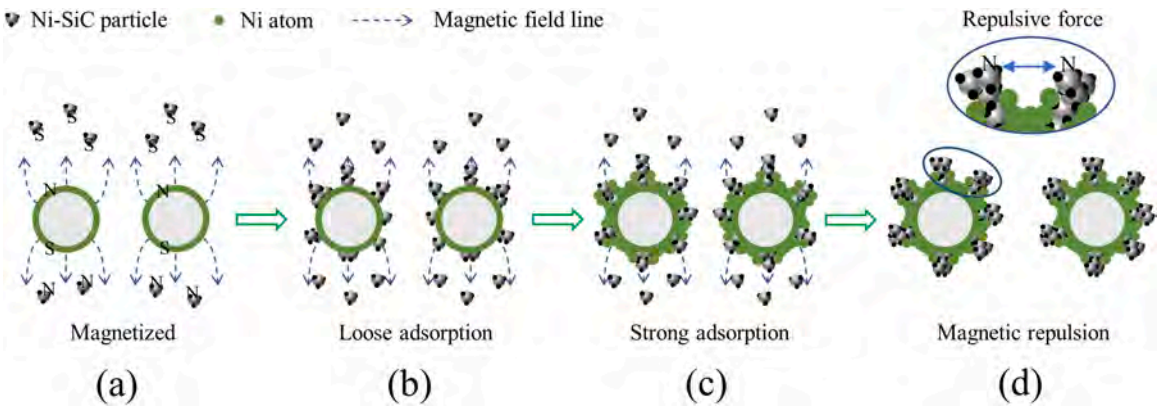

Fig. 5. Deposition mechanism of composite particles in magnetic field-assisted jet electrodeposition.

(Fig. 5c) [32–34]. In addition, upon the application of a magnetic field, the Ni-SiC clusters formed via localized stacking became magnetically polarized. The same magnetic pole was generated between adjacent clusters. Consequently, a magnetic repulsion was induced between the adjacent clusters, as shown in Fig. 5d. This magnetic repulsion promotes the radial growth of clusters along the mesh surface, resulting in a regular coral-like micro-nano hierarchical structure (Fig. 3b).

To understand the regular spacing of these structures, the magnetic interaction between clusters must be considered. As Ni-SiC clusters form via localized stacking, they become magnetically polarized with identical orientations. This induces a mutual magnetic repulsion between adjacent clusters (Fig. 5d). This repulsion prevents the clusters from merging into a solid mass, instead forcing them to grow radially and maintain a discrete, ordered distribution. The equilibrium between the attractive forces (driving height) and repulsive forces (driving spacing) ultimately results in the micro-nano hierarchical coral-like structure observed in Fig. 3b.

3.3. Surface wettability test

Surface wettability is a critical determinant of the mesh's oil/water separation performance [35]. The surface wettability of blank and Ni-SiC-coated meshes was tested in air and water environments, as shown in Fig. 6. Wettability testing of the stainless-steel mesh demonstrated a hydrophobic surface in air (WCA = 124.2°) and oleophobic behavior underwater (UOCA = 128.7°), as shown in Fig. 6a. However, the coating displayed superhydrophilicity in air, with a WCA of approximately 0°. As shown in Fig. 6b, the oil contact angle shifted to 159.9° once the Ni-SiC-coated mesh was submerged. This transition to underwater superoleophobicity results from the combination of the inherently hydrophilic SiC material and the high degree of surface roughness [21].

When the oil droplet was placed onto the mesh in an aqueous environment, a composite solid/water/oil interface was formed. The behavior of the underwater oil droplet is well-characterized by the Cassie-Baxter model [36], and the high UOCA is governed by the following equation:

$$\cos\theta'_{UOCA} = f\cos\theta_{UOCA} + f - 1 \tag{4}$$

where θ'_{UOCA} is the underwater oil contact angle on the rough surface, and θ_{UOCA} is the underwater oil contact angle on the smooth surface. f represents the solid area fraction, defined as the ratio of the actual contact area of the oil droplet to the total surface area [37]. In this work, θ_{UOCA} is 128.7°, θ'_{UOCA} is 159.9°, and f is 0.16 when DCE is used as oil sample. It is calculated that approximately 84% of the total contact area

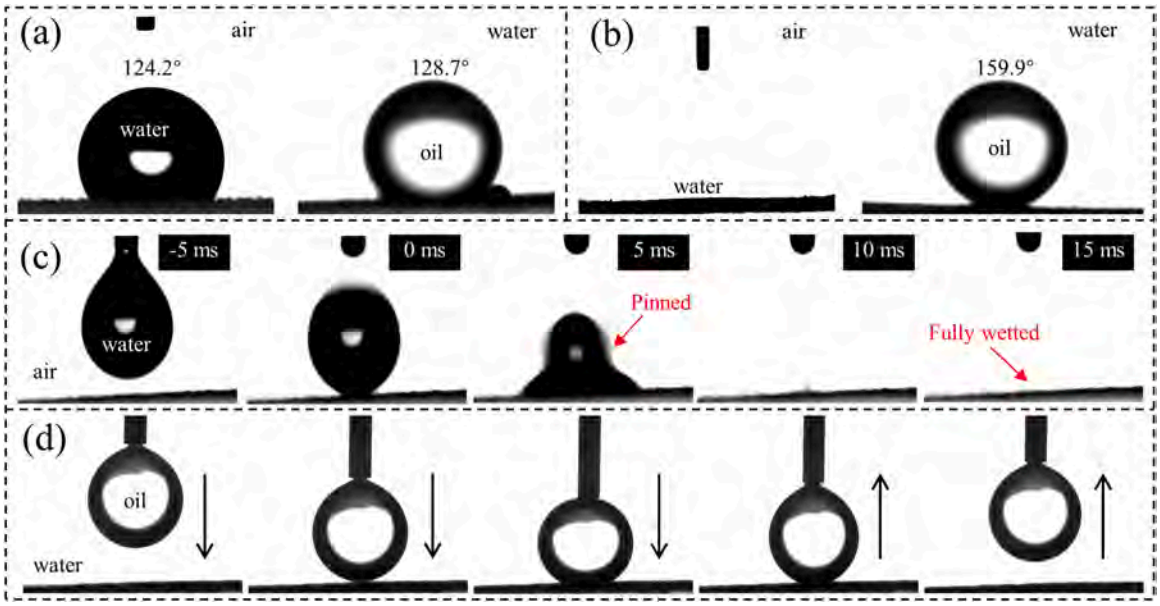

Fig. 6. Wettability of (a) blank mesh; (b) Ni-SiC composite coating mesh; (c) optical images of water droplet spreading on the Ni-SiC composite coating mesh; (d) underwater oil-adhesion test of the Ni-SiC composite coating mesh.

consists of the oil/water interface. Therefore, the Ni-SiC-coated mesh exhibits underwater superoleophobic properties.

The dynamic wetting process of a water droplet on the Ni-SiC composite coating mesh is shown in Fig. 6c. The Ni-SiC-coated mesh displayed affinities toward water according to the fast pinning and wetting behaviors of the impinging water drop on the mesh. Moreover, when an oil droplet was compressed against the Ni-SiC composite coating mesh surface, it underwent gradual deformation in response to increasing pressure. However, the oil droplet easily left the surface and recovered its spherical shape without sticking, as shown in Fig. 6d, indicating that the coating had an oil-repellent effect. The mesh surface forms a stable water film that acts as a physical barrier against oil fouling, thereby enhancing its separation performance. This mechanism is crucial for both separating oil/water mixtures and protecting the mesh from contamination.

3.4. Influence of electrodeposition time and voltage

3.4.1. Surface morphology and wettability of the Ni-SiC-coated mesh

Surface morphology of Ni-SiC-coated meshes prepared by different deposition times is presented in Fig. 7. The quantity of coatings increased with the increasing electrodeposition time accordingly. All mesh surfaces were covered by a nickel film with a thickness of approximately 0.92 μm. As shown in Fig. 7a and b, the mesh surface was sparsely distributed with a few Ni-SiC particles deposited for 10 min, and the height of the clusters on the mesh surface was 7.5 μm. As the deposition time increased to 20 min, the coral-like coating became noticeably denser, and the height of the clusters was increased to approximately 11.9 μm, as shown in Fig. 7d-f. The coating was denser, and the height of the clusters was further increased to 13.1 μm when the electrodeposition time was 30 min, as shown in Fig. 7g-i. Therefore, it can be concluded that a nickel film will rapidly form on the mesh surface at the initial stage of electrodeposition, and the density and height of the coating will gradually increase with the prolongation of electrodeposition time.

Fig. 8 shows the effect of electrodeposition time on the wettability of Ni-SiC-coated meshes. As electrodeposition time increased, the WCA and UOCA of the Ni-SiC-coated meshes gradually decreased and increased, respectively. At an electrodeposition time of 30 min, the Ni-SiC-coated mesh exhibited the WCA of 0° and the UOCA of 151.3°. These results demonstrate that the enhanced surface coverage associated with longer deposition times is critical for achieving superhydrophilicity and underwater superoleophobicity.

3.4.2. Effect of electrodeposition voltage on morphology and wettability

The morphology of the Ni-SiC-coated meshes at different applied voltages is presented in Fig. 9. When the electrodeposition voltage increased, the thickness of the nickel film on the mesh surface and the height of the coating clusters increased accordingly. Notably, by

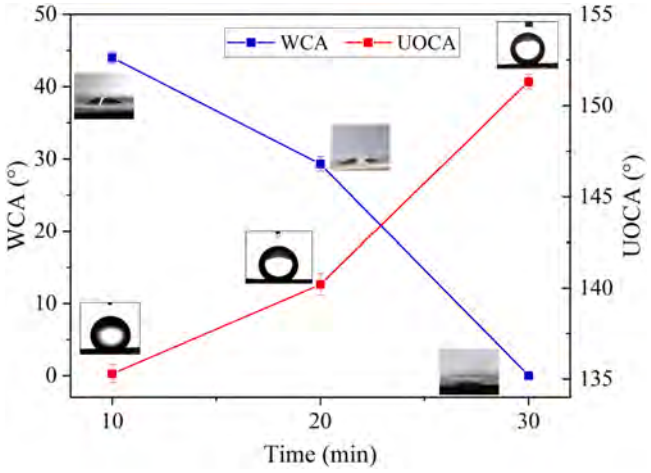

Fig. 8. The WCA and UOCA of the Ni-SiC-coated meshes electrodeposited at 10 V for 10, 20, and 30 min.

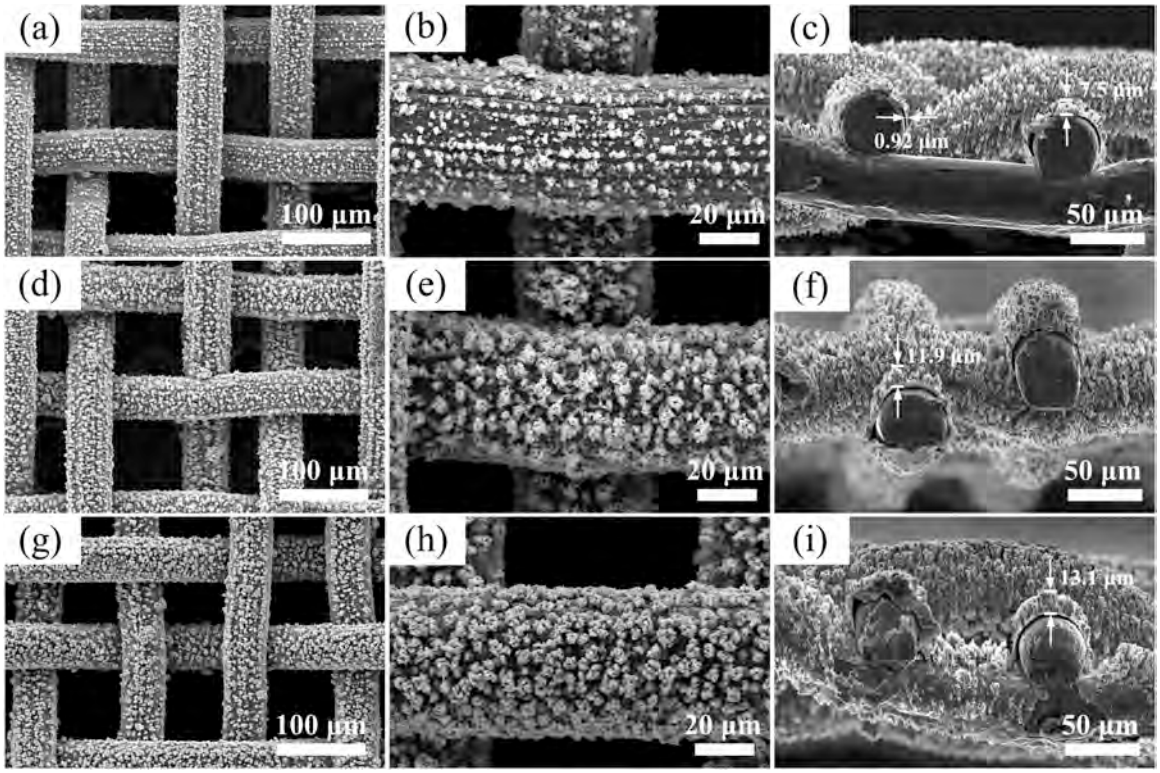

Fig. 7. Surface and cross-sectional morphology of the Ni-SiC-coated mesh for (a) 10 min, (b) 20 min, and (c) 30 min at 10 V.

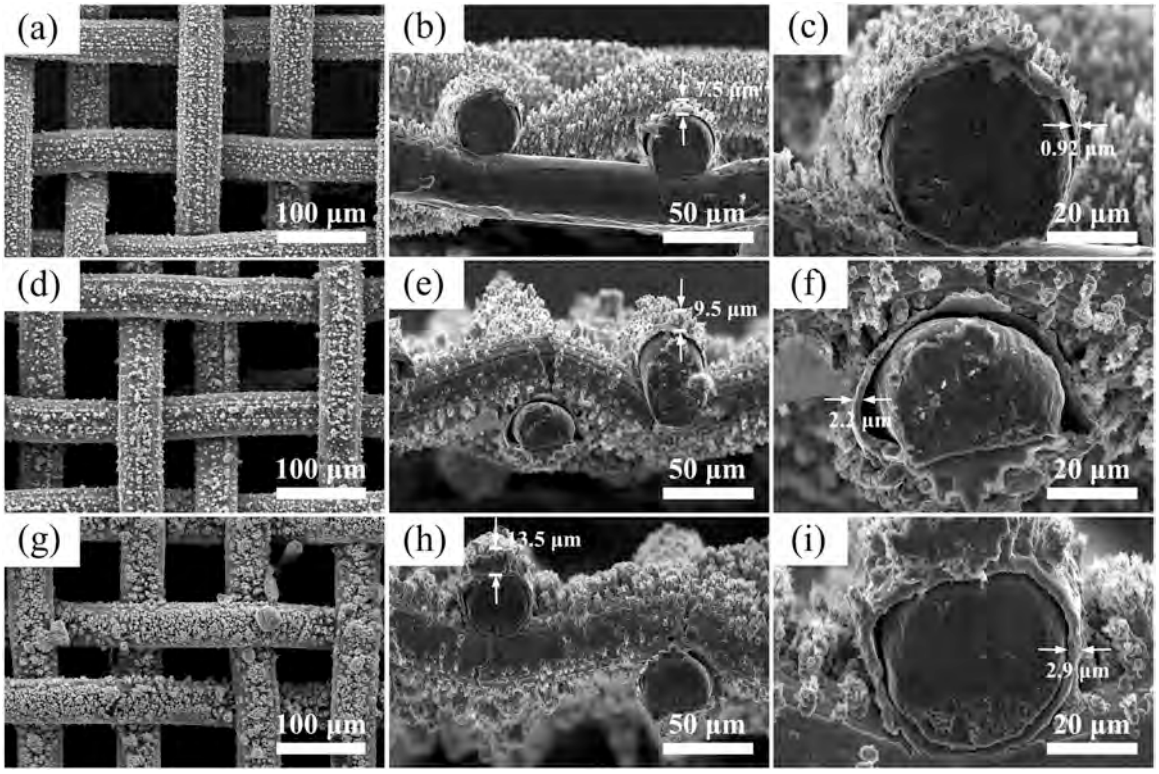

Fig. 9. Surface and cross-sectional morphology of the Ni-SiC-coated mesh at (a) 10 V, (b) 20 V, and (c) 30 V for 10 min.

increasing the voltage to 30 V, the height of the coating was significantly increased, leading to the formation of several larger clusters on the mesh surface, as presented in Fig. 9g. This behavior is consistent with Faraday's first law of electrolysis and can be attributed to the tip effect during the deposition process [38]. The high current density accelerated the deposition process, leading to the preferential reduction of metal ions at surface protrusions. This localized growth, driven by the tip effect, resulted in a distinct nodular morphology in the coating.

The effect of deposition voltage on the coating wettability is shown in Fig. 10. As with the electrodeposition time, the hydrophilicity and underwater oleophobicity were enhanced with increasing electrodeposition voltage. When the electrodeposition voltage increased to 30 V, the WCA and the UOCA declined to 0° and increased to 152.2°, respectively, indicating that the surface wetting behavior was governed by the specific morphological features of the coating.

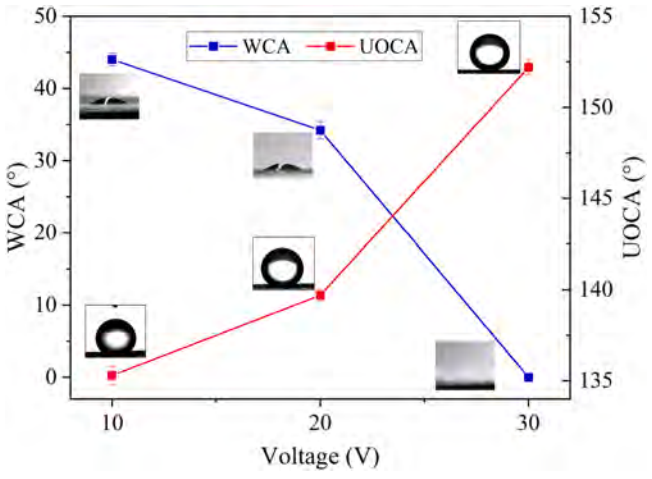

Fig. 10. The WCA and UOCA of the Ni-SiC-coated meshes electrodeposited at 10, 20, and 30 V for 10 min.

3.5. Oil/water separation test

As shown in Fig. 11a, the functionalized mesh was sandwiched between a pair of glass tubes to create the separation apparatus. The separation sequence is illustrated in Fig. 11b and c. Once the mesh was pre-wetted with water, a kerosene/water mixture was introduced into the upper tube. Due to the superhydrophilicity of the mesh, water quickly permeated through the surface and into the underlying beaker. Conversely, the underwater superoleophobicity caused the oil to be retained above the mesh, effectively preventing its passage.

The mechanism of the oil/water separation is governed by the synergistic superhydrophilicity and underwater superoleophobicity of the Ni-SiC-coated mesh. To further elucidate this mechanism, the capillary models depicted in Fig. 11e and f were employed. Each pore within the mesh serves as a channel for liquid penetration and can be modeled as a capillary tube. Consequently, the theoretical intrusion pressure (ΔP) for water and oil traversing the mesh can be determined using the following equations [39–41]:

$$\Delta P = 2\gamma/R = -\gamma L\cos\theta/A = -4\gamma\cos\theta/l \quad (5)$$

where γ represents the surface tension of liquid, R is the radius of curvature, and θ denotes the contact angle. Regarding the mesh geometry, L is the mesh perimeter, A represents the mesh surface area, and l donates the side length of the mesh opening (modeled as a square).

Fig. 11e shows that the superhydrophilicity of the mesh ($\theta < 90°$, $\Delta P < 0$) allows water to permeate the hierarchical structures spontaneously under the influence of gravity. This process establishes a stable water film that repels nonpolar oil due to its high polarity, achieving underwater superoleophobicity [18,42]. As a result, the oil contact angle exceeds 90° and ΔP becomes positive, as shown in Fig. 11f. This allows the mesh to support the oil phase under pressure, ensuring effective oil/water separation.

Water flux and oil intrusion pressure are two important properties of

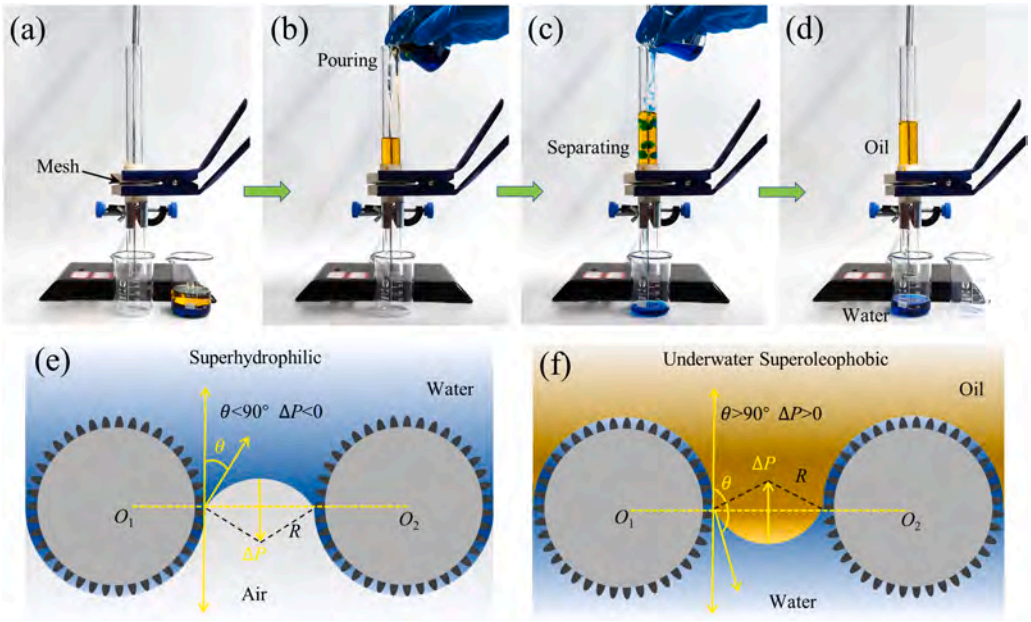

Fig. 11. (a-d) Oil/water separation test setup and testing process using the prepared mesh. Schematic illustration of the gravity-driven oil/water separation mechanism mediated by the superhydrophilic mesh: (e) superhydrophilicity in the air with $\Delta P < 0$; (f) underwater superoleophobicity with $\Delta P > 0$.

superhydrophilic meshes [43]. Fig. 12 illustrates the influence of mesh size on the water flux and the kerosene intrusion pressure. The corresponding permeate flux and oil intrusion pressure for the Ni-SiC-coated meshes were determined in accordance with Eqs. (2) and (3). All Ni-SiC-coated meshes are deposited using a 20 V voltage for 30 min. To determine the maximum hydrostatic height, kerosene was poured into a tube sealed with the Ni-SiC-coated mesh at its base. The breakthrough oil column height significantly increased from 64 mm to over 291 mm as the mesh count was raised from 100 to 500, demonstrating enhanced intrusion resistance at smaller pore sizes, as shown in Fig. 12a. Correspondingly, the oil intrusion pressure increased from 0.5 kPa to more than 2.28 kPa.

The time required for 120 mL of water to fully permeate the mesh was measured. Results indicated that the water flux decreased from 6.6×10^5 to 1.1×10^5 L • m^{-2} • h^{-1}as the mesh number increased, which was shown in Fig. 12b. The trend was consistent with Eq. (5).

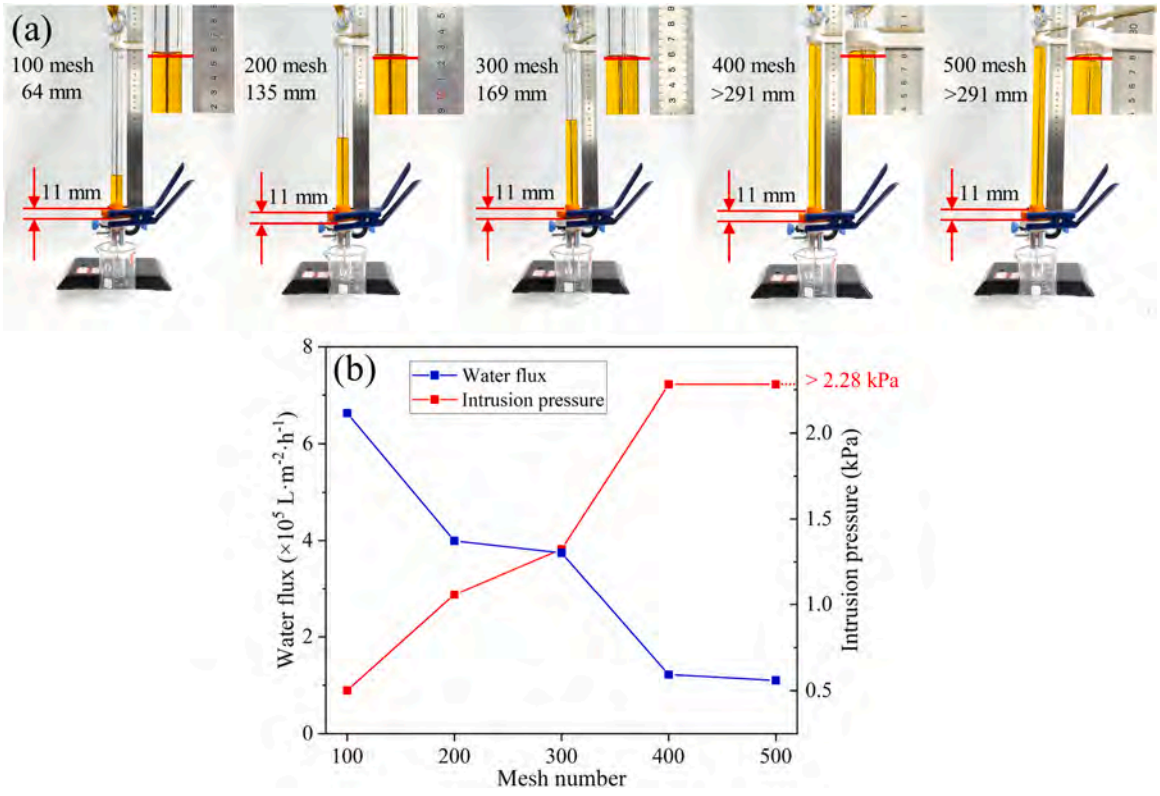

Fig. 12. Oil intrusion pressure and water flux testing of superhydrophilic meshes. (a) Oil column height, (b) intrusion pressure, and flux for different mesh numbers.

During the oil/water separation process, a higher mesh count (smaller pore size) resulted in increased oil intrusion pressure, thereby effectively preventing oil breakthrough. Conversely, the reduced pore dimensions also restricted the water permeation rate, leading to a decrease in the overall water flux. During oil/water separation, the prevention of oil leakage and the quick recovery of water are important. Therefore, a 300-mesh Ni-SiC-coated mesh was selected as the preferred sample for the subsequent separation test.

The separation ability of the Ni-SiC-coated mesh was investigated using a series of oils (hexane, kerosene, silicone oil, liquid paraffin, and DCE). As shown in Fig. 13a, the mesh achieved separation efficiencies above 95% for all mixtures, indicating its potential for broad practical use in oily wastewater treatment. While visible oil was absent in the permeate, a more rigorous analytical method was required to quantify the separation purity. Consequently, the total organic carbon concentration in the collected water was measured to evaluate the residual oil content and overall separation efficiency. The oil content in the collected water was all less than 16.5 mg/L, as shown in Fig. 13a. Furthermore, the reusability and cyclic stability of the Ni-SiC-coated mesh were evaluated. Following each separation cycle, the mesh was rinsed with deionized water to regenerate its surface. As demonstrated in Fig. 13b, the separation efficiency remained consistently above 95% even after 50 cycles, confirming the outstanding durability and practical recycling potential of the coating.

3.6. Material stability

The durability of oil/water separation meshes is critical for practical deployment. Thus, the chemical stability of the Ni-SiC-coated mesh was evaluated across acidic, alkaline, and saline environments. Following immersion in 1 M HCl, 1 M NaOH, and saturated NaCl solutions for varying soak times, the UOCA consistently remained above 150° with only minor fluctuations, as shown in Fig. 14a, demonstrating excellent corrosion resistance. The separation performance of the Ni-SiC-coated mesh after 2 h of immersion in various corrosive solutions is illustrated in Fig. 14b. As mentioned above, the hydrophilic SiC material exhibited stable chemical properties [28], which endowed the prepared superhydrophilic mesh with stability in corrosive environments. When the oil/solution mixture contacted the mesh pre-wetted with water, the solution rapidly fused with the water to form a stable solution layer to block the intrusion of oil, as shown in Fig. 14c. These results collectively demonstrate that the Ni-SiC-coated mesh possesses exceptional corrosion resistance and underwater superoleophobicity in acidic, alkaline, and hypersaline environments. Such chemical robustness highlights the practical potential of this superhydrophilic mesh for treating complex oily wastewater under harsh conditions.

In addition, oil/water separation meshes are inevitably subjected to water erosion in practical applications. Therefore, their mechanical stability under dynamic hydraulic conditions is a key indicator for evaluating their actual service performance. To evaluate the mechanical stability of the Ni-SiC-coated mesh in a flowing water environment, a water erosion test was designed, with an erosion flow rate of 360 L/h. Fig. 15a shows the changes in the UOCA of the mesh surface after different erosion times. The results showed that the UOCA of the Ni-SiC-coated mesh remained above 155° at all erosion time points, indicating that it maintained excellent superoleophobic properties and structural robustness under continuous water flow impact. Further, Fig. 15b shows the separation efficiency of the Ni-SiC-coated mesh for the kerosene after water erosion for different times. The results showed that even after 10 h of continuous water erosion, the Ni-SiC-coated mesh still achieved a kerosene separation efficiency of over 95%, which was similar to its initial separation efficiency. This indicates that the coated membrane has good mechanical stability and separation performance retention under water erosion.

It was reported that hydrophilic materials are highly susceptible to fouling by airborne organic contaminants. During long-term storage in air, the surface wettability gradually transitions from its initial hydrophilicity to hydrophobicity, and eventually to superhydrophobicity. This unfavorable shift significantly impairs permeate flux and overall separation performance [44–46]. Thus, the environmental durability of the Ni-SiC-coated mesh was studied. The Ni-SiC-coated mesh still exhibited excellent superhydrophilicity and underwater superoleophobicity after being stored under ambient conditions for three months, demonstrating the excellent stability of the Ni-SiC-coated mesh for long-term storage. With its sustained low oil-adhesion and environmental robustness, the Ni-SiC-coated mesh is a highly promising candidate for industrial-scale oil/water separation under challenging conditions.

4. Conclusion

A Ni-SiC composited coating stainless-steel mesh was prepared via efficient magnetic-field-assisted jet electrodeposition. Under the influence of an external magnetic field, the coating developed a coral-like micro/nano-hierarchical structure, significantly increasing the surface roughness. The Ni-SiC-coated mesh exhibited outstanding superhydrophilicity and underwater superoleophobicity. The influence of

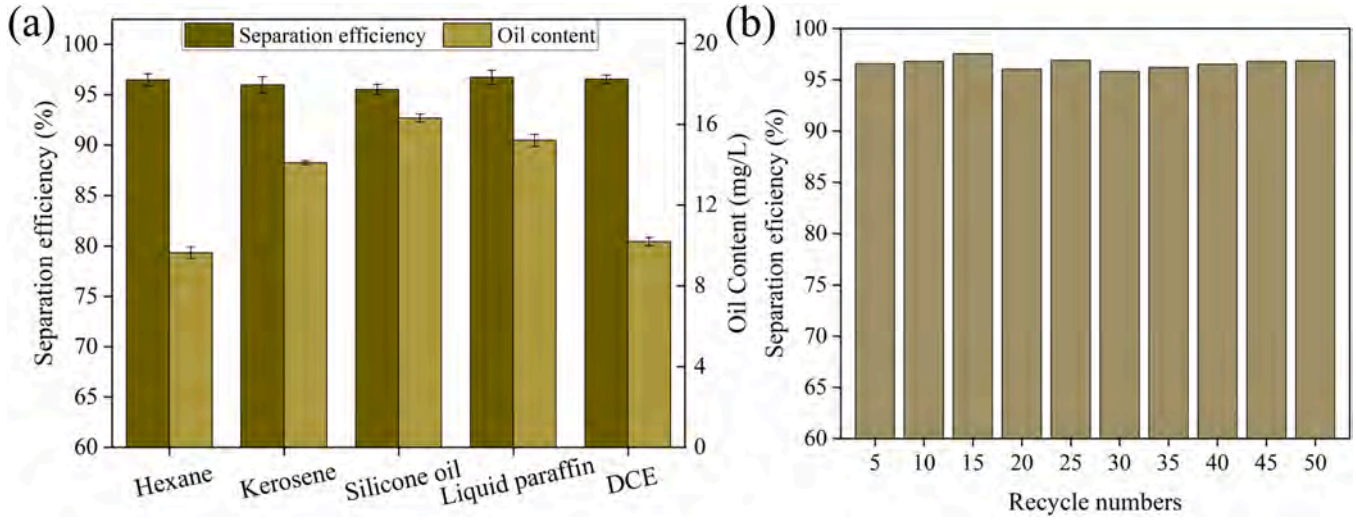

Fig. 13. (a) Oil/water separation efficiency of the Ni-SiC-coated mesh and oil content in collected water; (b) The separation efficiency of the prepared mesh after multiple cycles of separation (using kerosene as an example).

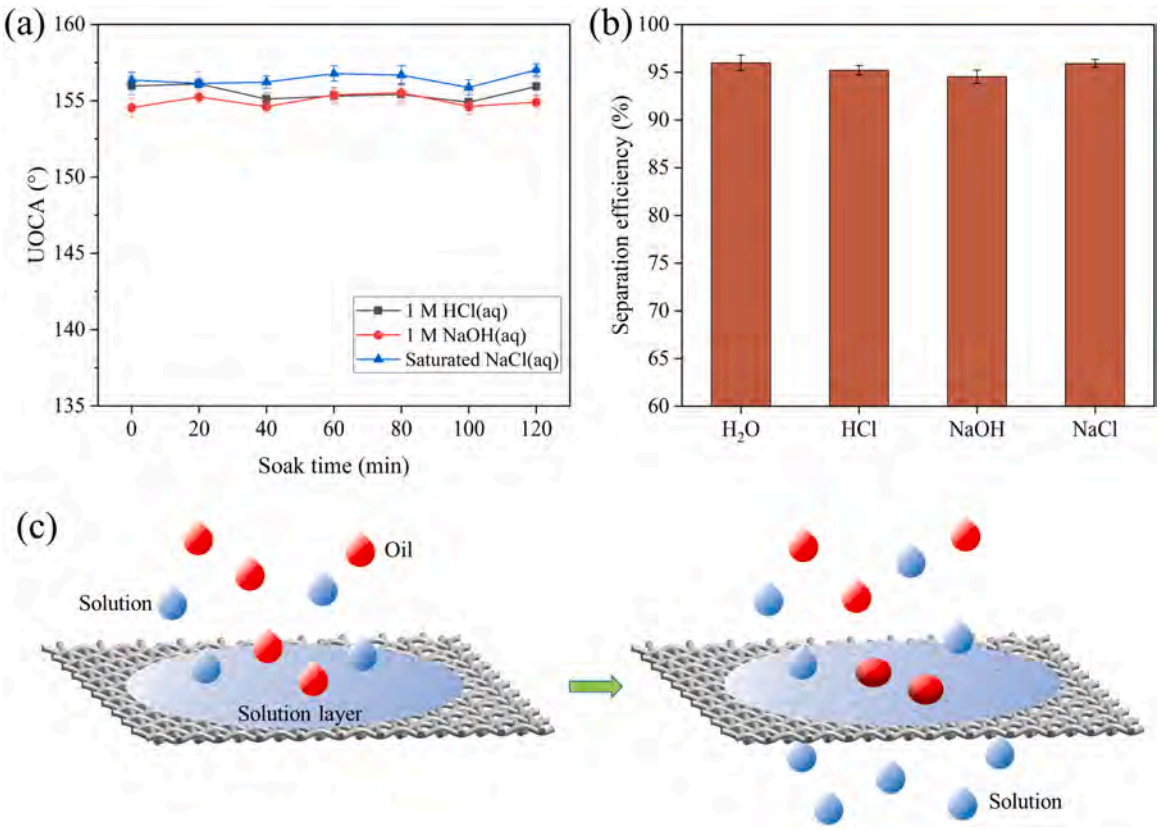

Fig. 14. Stability in different corrosive solutions. (a) UOCA after immersion in corrosive solutions for different times, (b) the oil/solution separation efficiencies after immersion in corrosive solutions, and (c) the mechanism of the oil/solution separation process.

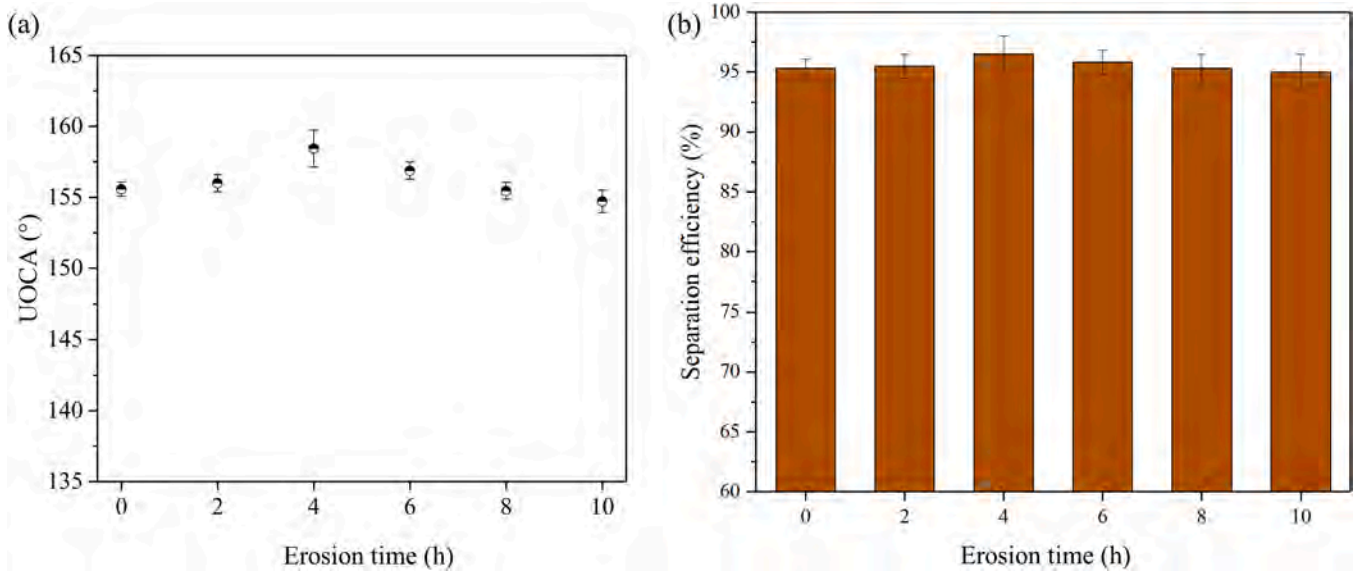

Fig. 15. Stability after water erosion. (a) UOCA after water erosion for different times, (b) separation efficiency after water erosion for different times (using kerosene as an example).

deposition time and applied voltage on the surface morphology and wettability of the mesh was investigated. Appropriate process parameters were selected to prepare samples for oil/water separation. The results showed that the Ni-SiC-coated mesh exhibited excellent oil/water separation performance and could achieve high-purity separation more than 50 times for various oil/water mixtures. Besides, the material stability test results showed that the Ni-SiC-coated mesh could maintain stable oil/water separation performance in acid, alkali, and salt environments. Furthermore, following three months of exposure to ambient air, the Ni-SiC-coated mesh still exhibited excellent superhydrophilicity and underwater superoleophobicity. Thus, the developed Ni-SiC-coated mesh represents a promising candidate for the remediation of complex industrial oily wastewater and the mitigation of large-scale oil spills. The Ni-SiC-coated mesh can maintain underwater superhydrophobicity and

achieve a separation efficiency of over 95% after erosion with a water flow rate of 360 L/h for 10 h.

CRediT authorship contribution statement

Zongjun Tian: Writing – review & editing, Supervision, Resources, Project administration, Funding acquisition. **Shimao Shangguan:** Writing – original draft, Visualization, Data curation. **Haozhe Pang:** Writing – original draft, Investigation, Formal analysis, Data curation. **Ya Chen:** Writing – review & editing, Writing – original draft, Methodology, Investigation, Funding acquisition, Formal analysis, Data curation, Conceptualization. **Sarat Singamneni:** Writing – review & editing, Validation, Resources, Investigation. **Jianfeng Zhao:** Writing – review & editing, Investigation, Formal analysis. **Wuxin Yang:** Writing – review & editing, Writing – original draft, Investigation, Formal analysis, Data curation, Conceptualization.

Declaration of Competing Interest

The authors declare that they have no known competing financial interests or personal relationships that could have appeared to influence the work reported in this paper.

Acknowledgements

This work was supported by the National Natural Science Foundation of China (No. 52275433).

Data availability

Data will be made available on request.

References

[1] J.H. Grabowski, S.P. Powers, H. Roman, S. Rouhani, Potential impacts of the 2010 Deepwater Horizon oil spill on subtidal oysters in the Gulf of Mexico, Mar. Ecol. Prog. Ser. 576 (2017) 163–174, https://doi.org/10.3354/meps12208.
[2] M.A. Shannon, P.W. Bohn, M. Elimelech, J.G. Georgiadis, B.J. Mariñas, A. M. Mayes, Science and technology for water purification in the coming decades, Nature 452 (2008) 301–310, https://doi.org/10.1038/nature06599.
[3] Y. Zhang, H. Wang, X. Wang, B. Liu, Y. Wei, An anti-oil-fouling and robust superhydrophilic MnCo2O4 coated stainless steel mesh for ultrafast oil/water mixtures separation, Sep. Purif. Tech. 264 (2021) 118435, https://doi.org/10.1016/j.seppur.2021.118435.
[4] J. Wang, S. Liu, S. Guo, Calcium ions enhanced mussel-inspired underwater superoleophobic coating with superior mechanical stability and hot water repellence for efficient oil/water separation, Appl. Surf. Sci. 503 (2020) 144180, https://doi.org/10.1016/j.apsusc.2019.144180.
[5] S. Xu, Q. Wang, N. Wang, Fabrication of pre-wetting induced superamphiphobic meshes for on-demand oil-water separation of light or heavy oil-water mixtures, Colloids Surf. A Physicochem. Eng. Asp. 602 (2020) 125095, https://doi.org/10.1016/j.colsurfa.2020.125095.
[6] H. Duan, H. Lyu, B. Shen, J. Tian, X. Pu, F. Wang, X. Wang, Superhydrophobic-superoleophilic biochar-based foam for high-efficiency and repeatable oil-water separation, Sci. Total Environ. 780 (2021) 146517, https://doi.org/10.1016/j.scitotenv.2021.146517.
[7] J. Lu, X. Liu, T.C. Zhang, H. He, S. Yuan, Magnetic superhydrophobic polyurethane sponge modified with bioinspired stearic acid@Fe3O4@PDA nanocomposites for oil/ water separation, Colloids Surf. A Physicochem. Eng. Asp. 624 (2021) 126794, https://doi.org/10.1016/j.colsurfa.2021.126794.
[8] L. Zhang, X. Yang, B. Jiang, Y. Sun, Z. Gong, N. Zhang, S. Hou, J. Li, N. Yang, Superhydrophilic and underwater superoleophobic Ti foam with robust nanoarray structures of TiO2 for effective oil-in-water emulsion separation, Sep. Purif. Tech. 252 (2020) 117437, https://doi.org/10.1016/j.seppur.2020.117437.
[9] Y. Chen, A. Xie, J. Cui, J. Lang, C. Li, Y. Yan, J. Dai, One-step facile fabrication of visible light driven antifouling carbon cloth fibers membrane for efficient oil-water separation, Sep. Purif. Tech. 228 (2019) 115769, https://doi.org/10.1016/j.seppur.2019.115769.
[10] Z.X. Xue, M.J. Liu, L. Jiang, Recent developments in polymeric superoleophobic surfaces, J. Polym. Sci. Part B Polym. Phys. 50 (2012) 1209–1224, https://doi.org/10.1002/polb.23115.
[11] M. Wang, D. Hu, Y. Li, H. Peng, J. Zeng, Biobased mussel-inspired underwater superoleophobic chitosan derived complex hydrogel coated cotton fabric for oil/water separation, Int. J. Biol. Macromol. 209 (2022) 279–289, https://doi.org/10.1016/j.ijbiomac.2022.04.007.
[12] H. He, T.C. Zhang, Z. Li, Y. Liang, S. Yuan, Superhydrophilic fish-scale-like CuC2O4 nanosheets wrapped copper mesh with underwater super oil-repellent properties for effective separation of oil-in-water emulsions, Colloids Surf. A Physicochem. Eng. Asp. 627 (2021) 127133, https://doi.org/10.1016/j.colsurfa.2021.127133.
[13] D.Y. Gao, Z. Liu, Z.L. Cheng, Superhydrophilic and underwater superoleophobic in-situ derived 2D Ni-Fe MOF/HNTs composite-enhanced polyvinyl alcohol (PVA) hydrogel membrane for gravity-driven oil/water separation, J. Environ. Chem. Eng. 10 (2022) 107904, https://doi.org/10.1016/j.jece.2022.107904.
[14] J.L. Zhang, X.F. Huang, Y.J. Xiong, W.W. Zheng, W.Q. Liu, M.F. He, L.X. Li, J. Liu, L.J. Lu, K.M. Peng, Spider silk bioinspired superhydrophilic nanofibrous membrane for efficient oil/water separation of nanoemulsions, Sep. Purif. Tech. 280 (2022) 119824, https://doi.org/10.1016/j.seppur.2021.119824.
[15] X.Y. Yin, Y. He, H.J. Li, X.Y. Ma, L. Zhou, T. He, S.S. Li, One-step in-situ fabrication of carbon nanotube/stainless steel mesh membrane with excellent anti-fouling properties for effective gravity-driven filtration of oil-in-water emulsions, J. Colloid Interface Sci. 592 (2021) 87–94, https://doi.org/10.1016/j.jcis.2021.02.043.
[16] Y.Q. Wang, Y. He, H.J. Li, J. Yu, L.Y. Zhang, L. Chen, Y. Bai, Layer-by-layer construction of CS-CNCs multilayer modified mesh with robust anti-crude-oil-fouling performance for efficient oil/water separation, J. Membr. Sci. 639 (2021) 119776, https://doi.org/10.1016/j.memsci.2021.119776.
[17] Z.-Y. Luo, K.-X. Chen, Y.-Q. Wang, J.-H. Wang, D.-C. Mo, S.-S. Lyu, Superhydrophilic Nickel Nanoparticles with Core–Shell Structure To Decorate Copper Mesh for Efficient Oil/Water Separation, J. Phys. Chem. C. 120 (2016) 12685–12692, https://doi.org/10.1021/acs.jpcc.6b03940.
[18] X. Gou, X. Yu, Y. Liu, L. Wang, Y. He, D. Tian, F. Shen, G. Yang, X. Zhang, Y. Zhang, 3D antifouling hierarchical micro/nanostructures with underwater superoleophobicity via one-step electrodeposition on anode and cathode, Surf. Coat. Technol. 421 (2021) 127356, https://doi.org/10.1016/j.surfcoat.2021.127356.
[19] L. Shen, M. Xu, W. Jiang, M. Qiu, M. Fan, G. Ji, Z. Tian, A novel superhydrophobic Ni/Nip coating fabricated by magnetic field induced selective scanning electrodeposition, Appl. Surf. Sci. 489 (2019) 25–33, https://doi.org/10.1016/j.apsusc.2019.05.335.
[20] F. Xia, W. Jia, M. Jiang, W. Cui, J. Wang, Microstructure and corrosion properties of Ni-TiN nanocoatings prepared by jet pulse electrodeposition, Ceram. Int. 43 (2017) 14623–14628, https://doi.org/10.1016/j.ceramint.2017.07.117.
[21] H. Du, F. Liu, H. Wang, Bio-inspired robust superhydrophilic/underwater superoleophobic coating with lubrication, anti-crude oil fouling and anti-corrosion performances, J. Colloid Interface Sci. 616 (2022) 720–729, https://doi.org/10.1016/j.jcis.2022.02.090.
[22] M.A. Gondal, M.S. Sadullah, M.A. Dastageer, G.H. McKinley, D. Panchanathan, K. K. Varanasi, Study of factors governing oil–water separation process using TiO2 films prepared by spray deposition of nanoparticle dispersions, ACS Appl. Mater. Interfaces 6 (2014) 13422–13429, https://doi.org/10.1021/am501867b.
[23] U.B. Gunatilake, J. Bandara, Fabrication of highly hydrophilic filter using natural and hydrothermally treated mica nanoparticles for efficient waste oil-water separation, J. Environ. Manag. 191 (2017) 96–104, https://doi.org/10.1016/j.jenvman.2017.01.002.
[24] L.H. Zhang, Z.Q. Gong, B. Jiang, Y.L. Sun, Z.X. Chen, X. Gao, N. Yang, Ni-Al layered double hydroxides (LDHs) coated superhydrophobic mesh with flower-like hierarchical structure for oil/water separation, Appl. Surf. Sci. 490 (2019) 145–156, https://doi.org/10.1016/j.apsusc.2019.06.064.
[25] B.S. Li, W.W. Zhang, D.D. Li, J.J. Wang, W. Chen, Y.Y. Liu, Preparation of Ni-W/TiN-Y2O3 composite ceramic coating for metallic parts protection by direct current deposition, Ceram. Int. 45 (2019) 13242–13250, https://doi.org/10.1016/j.ceramint.2019.04.010.
[26] Z.-Y. Luo, S.-S. Lyu, Y.-X. Fu, Y. Heng, D.-C. Mo, The Janus effect on superhydrophilic Cu mesh decorated with Ni-NiO/Ni(OH)2 core-shell nanoparticles for oil/water separation, Appl. Surf. Sci. 409 (2017) 431–437, https://doi.org/10.1016/j.apsusc.2017.03.078.
[27] J. Xu, Y. Chen, L. Shen, J. Zhao, G. Lou, D. Huang, Y. Yang, Fabrication of superhydrophobic stainless-steel mesh for oil-water separation by jet electrodeposition, Colloids Surf. A Physicochem. Eng. Asp. 649 (2022) 129434, https://doi.org/10.1016/j.colsurfa.2022.129434.
[28] T. Xiao, J. Kuang, P. Sun, X. Hou, Q. Wang, P. Jiang, W. Cao, Rapid microwave synthesis of coaxial SiC/carbon fibre (SiC/CF) with improved oxidation resistance and wettability, Ceram. Int. 45 (2019) 2432–2438, https://doi.org/10.1016/j.ceramint.2018.10.167.
[29] J. Li, R. Kang, X. Tang, H. She, Y. Yang, F. Zha, Superhydrophobic meshes that can repel hot water and strong corrosive liquids used for efficient gravity-driven oil/water separation, Nanoscale 8 (2016) 7638–7645, https://doi.org/10.1039/C6NR01298A.
[30] Z.X. Xue, S.T. Wang, L. Lin, L. Chen, M.J. Liu, L. Feng, L. Jiang, A novel superhydrophilic and underwater superoleophobic hydrogel-coated mesh for oil/water separation, Adv. Mater. 23 (2011) 4270–4273, https://doi.org/10.1002/adma.201102616.
[31] L. Shen, M. Fan, M. Qiu, W. Jiang, Z. Wang, Superhydrophobic nickel coating fabricated by scanning electrodeposition, Appl. Surf. Sci. 483 (2019) 706–712, https://doi.org/10.1016/j.apsusc.2019.04.019.
[32] H. Ness, F. Gautier, Theoretical study of the interaction between a magnetic nanotip and a magnetic surface, Phys. Rev. B 52 (1995) 7352–7362, https://doi.org/10.1103/PhysRevB.52.7352.
[33] H.A. Stone, J.R. Lister, M.P. Brenner, Drops with conical ends in electric and magnetic fields, Proc. Math. Phys. Eng. Sci. 455 (1999) 329–347, https://doi.org/10.1098/rspa.1999.0316.

[34] J.V.I. Timonen, M. Latikka, L. Leibler, R.H.A. Ras, O. Ikkala, Switchable static and dynamic self-assembly of magnetic droplets on superhydrophobic surfaces, Science 341 (2013) 253–257, https://doi.org/10.1126/science.1233775.
[35] F. Wahid, X.-Q. Zhao, J.-X. Cui, Y.-Y. Wang, F.-P. Wang, S.-R. Jia, C. Zhong, Fabrication of bacterial cellulose with TiO2-ZnO nanocomposites as a multifunctional membrane for water remediation, J. Colloid Interface Sci. 620 (2022) 1–13, https://doi.org/10.1016/j.jcis.2022.03.108.
[36] M. Liu, S. Wang, Z. Wei, Y. Song, L. Jiang, Bioinspired design of a superoleophobic and low adhesive water/solid interface, Adv. Mater. 21 (2009) 665–669, https://doi.org/10.1002/adma.200801782.
[37] J. Li, L. Yan, H. Li, W. Li, F. Zha, Z. Lei, Underwater superoleophobic palygorskite coated meshes for efficient oil/water separation, J. Mater. Chem. A 3 (2015) 14696–14702, https://doi.org/10.1039/C5TA02870A.
[38] X. Guo, T. Zhang, J. Li, T. Fan, Butterfly-scale architecture directed electrodeposition of Ag microband arrays for electrochemical detection, RSC Adv. 4 (2014) 59508–59512, https://doi.org/10.1039/C4RA11189C.
[39] H. Gao, Y. Liu, G. Wang, S. Li, Z. Han, L. Ren, Switchable wettability surface with chemical stability and antifouling properties for controllable oil–water separation, Langmuir 35 (2019) 4498–4508, https://doi.org/10.1021/acs.langmuir.9b00094.
[40] L. Qiu, Y.H. Sun, Z.G. Guo, Designing novel superwetting surfaces for high-efficiency oil-water separation: design principles, opportunities, trends and challenges, J. Mater. Chem. A 8 (2020) 16831–16853, https://doi.org/10.1039/d0ta02997a.
[41] X. Lin, J. Hong, Recent advances in robust superwettable membranes for oil-water separation, Adv. Mater. Interfaces 6 (2019) 1900126, https://doi.org/10.1002/admi.201900126.
[42] C. Zhou, J. Cheng, K. Hou, Z. Zhu, Y. Zheng, Preparation of CuWO4@Cu2O film on copper mesh by anodization for oil/water separation and aqueous pollutant degradation, Chem. Eng. J. 307 (2017) 803–811, https://doi.org/10.1016/j.cej.2016.08.119.
[43] Z. Wang, C. Xiao, Z. Wu, Y. Wang, X. Du, W. Kong, D. Pan, G. Guan, X. Hao, A novel 3D porous modified material with cage-like structure: fabrication and its demulsification effect for efficient oil/water separation, J. Mater. Chem. A 5 (2017) 5895–5904, https://doi.org/10.1039/C6TA10248D.
[44] Z. Yang, X. Liu, Y. Tian, Insights into the wettability transition of nanosecond laser ablated surface under ambient air exposure, J. Colloid Interface Sci. 533 (2019) 268–277, https://doi.org/10.1016/j.jcis.2018.08.082.
[45] W. Guo, B. Chen, V.L. Do, G.H. ten Brink, B.J. Kooi, V.B. Svetovoy, G. Palasantzas, Effect of airborne hydrocarbons on the wettability of phase change nanoparticle decorated surfaces, ACS Nano 13 (2019) 13430–13438, https://doi.org/10.1021/acsnano.9b06909.
[46] X. Li, Y. Jiang, Z. Jiang, Y. Li, C. Wen, J. Lian, Reversible wettability transition between superhydrophilicity and superhydrophobicity through alternate heating-reheating cycle on laser-ablated brass surface, Appl. Surf. Sci. 492 (2019) 349–361, https://doi.org/10.1016/j.apsusc.2019.06.145.